

See discussions, stats, and author profiles for this publication at: <https://www.researchgate.net/publication/258683774>

On the Measurements of Rigidity Modulus of Soft Materials in Nanoindentation Experiments at Small Depth

ARTICLE *in* MACROMOLECULES · MAY 2012

Impact Factor: 5.8 · DOI: 10.1021/ma202600b

CITATIONS

33

READS

88

2 AUTHORS, INCLUDING:



Igor Sokolov

Tufts University

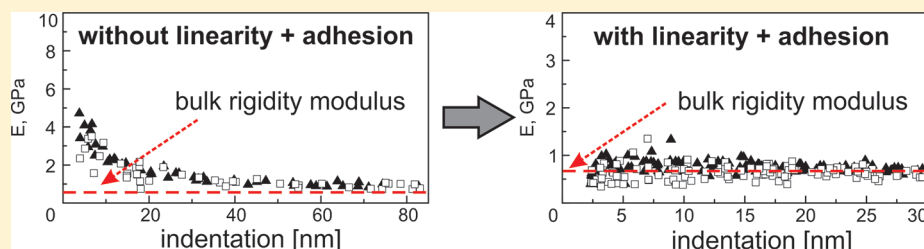
179 PUBLICATIONS 3,457 CITATIONS

SEE PROFILE

On the Measurements of Rigidity Modulus of Soft Materials in Nanoindentation Experiments at Small Depth

Maxim E. Dokukin[†] and Igor Sokolov^{†,‡,*}

[†]Department of Physics and [‡]Nanoengineering and Biotechnology Laboratories Center (NABLAB), Clarkson University, Potsdam, New York 13699-5820, United States



ABSTRACT: It is of interest to measure the modulus of rigidity at small indentation depths for many systems, such as thin films, nanocomposites, biomaterials, etc. Depth-dependence of the rigidity modulus of homogeneous soft materials is broadly observed in nanoindentation experiments. Typically, the modulus reaches its bulk value only when the indentation depth becomes relatively large. Nature of this effect (we suggest to call this “skin-effect” for short) is not well understood. It is not even clear if this is a real effect or an artifact. Here we present the results of precise indentation measurements based on the use of atomic force microscopy (AFM), which suggest that the skin-effect may be an artifact. It can be eliminated, and the bulk modulus can be measured at nanometer indentations if one (a) takes into account adhesion between the indenter and surface of interest, and (b) operates mostly within the linear stress–strain regime. To demonstrate it, we used three AFM probes of well-defined geometry (radii of the apex were 22, 810, and 1030 nm) to study the indentation of three different polymers of the bulk rigidity of 0.6–0.7 GPa (polyurethanes) and 2.8 GPa (polystyrene). The obtained force–indentation curves were processed through the Oliver–Pharr, Hertz, Johnson–Kendall–Roberts (JKR) and Derjaguin–Muller–Toporov (DMT) models. We found that the skin-effect disappeared when using dull (810 and 1030 nm) probes and processing the force–deformation data with either of the adhesion models (JKR or DMT). Moreover, the measured moduli were independent of the indentation depth. The values of the rigidity modulus were very close to the bulk values starting from the indentations of 2–3 nm. Such a small indentation seems to be the smallest one for soft materials at which the bulk modulus has been reached. When using the sharp (22 nm) probe, we were not able to reach the bulk moduli up to the maximum possible indentation allowed by the instrument 90 nm. The other sources of possible error in the modulus measurements are discussed. We conclude that the skin-effect originates mainly at both nonlinearity of stress–strain relation (occurs when using excessively sharp probes) and if the probe–surface adhesion is not taken into account (like in Oliver–Pharr and Hertz models).

INTRODUCTION

With the development of nanoindentation techniques,^{1–3} it has become possible to study mechanics of polymers, nanocomposites, biomaterials, single biological cells and tissues at the nanoscale. The study of nanomechanical properties of polymeric polishing pads is important in semiconductor industry.^{4–6} Superior properties of bionano-composite materials, for example Abalone shell, have been known for decades; whereas its nanomechanical properties were studied just recently.⁷ Recent studies of mechanics of cells at the nanoscale revealed its correlation with a number of various diseases and even aging.^{8–13} Indentation is a versatile method which can easily be extended from nano- to macro-scale.^{14,15} The methods for indentation analysis are well-known and could be used for a wide variety of systems like homogeneous¹⁶ or composites materials,^{17–19} films,^{19–25} and live organisms.^{10,26,27}

There are two major probe indentation techniques currently available: nanoindenter and atomic force microscopy (AFM).

Both techniques allow recording force–penetration (or hereafter force–indentation) curves. Nanoindenters are nowadays standard instruments used to study mechanics of materials at the nanoscale. Nonetheless, AFM has been widely used to probe nanomechanical properties for the last 20 years.^{22,28–31} When measuring rigid materials, nanoindenting is a more convenient and typically more accurate method compared to AFM. AFM is more preferable when studying soft materials because it can operate with smaller forces compared to nanoindenters.

It is still a serious challenge for both techniques to do quantitative measurements on soft viscoelastic materials at the nanoscale.^{32–38} Both methods have numerous problems related to the cantilever calibration, identification of the point of contact, probe geometry, cantilever spring constant, sample

Received: December 1, 2011

Revised: April 23, 2012

Macromolecules, 2012, 45 (10), pp 4277–4288

dx.doi.org/10.1021/ma202600b | Macromolecules XXXX, XXX, XXX–XXX



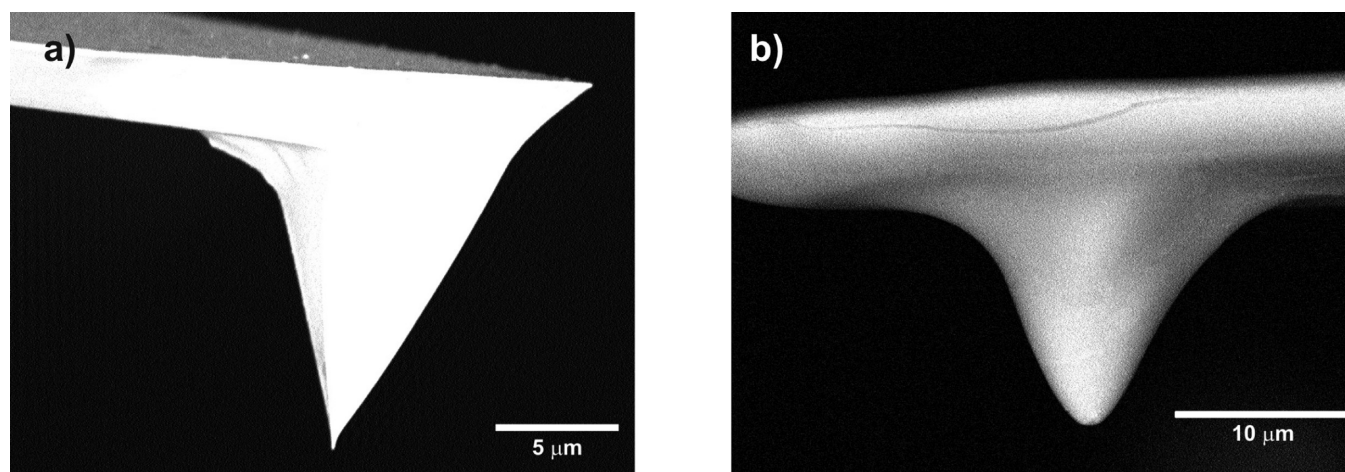


Figure 1. SEM images of AFM probes used as indenters in the present work: (a) a standard RTESP probe; (b) an annealed dull probe.

creep, etc.³⁹ The nanoindenter data are typically processed through a model suitable for the indenters of arbitrary shape (Oliver and Pharr^{40,41}). Viscoelastic behavior of materials can also be taken into account.^{42–45} The AFM data can usually be processed through a larger variety of models (like Hertz,⁴⁶ Derjaguin–Muller–Toporov (DMT),⁴⁷ Johnson–Kendall–Roberts (JKR),⁴⁸ Maugis,^{49–52} etc.) which rely on the use of a spherical probe, and can take the probe-sample adhesion into account.

It was broadly observed in nanoindentation experiments that the rigidity modulus of supposed-to-be-homogeneous soft materials depends on the indentation depth at the nanoscale.^{22,24,33,37,38,40,45,53–56} The modulus measured, being usually higher than the bulk rigidity near the surface, reaches its bulk value with the increase of indentation. It should be noted that there is somewhat similar effect observed on the rigid materials, metals, which is called “the indentation size effect (ISE)”.⁵⁷ The nature of that effect is rather clear; it has been attributed to the evolution of the so-called geometrically necessary dislocations beneath the indenter and contribution of defects in general. This argumentation is not applicable for homogeneous defect free soft materials. Therefore, we suggest calling this effect for soft materials “*skin effect*” for short.

The overevaluated rigidity modulus at a small indentation depth was found for the case of the Oliver–Pharr method.^{38,53,54} It was initially suggested that it might be due to the insufficient knowledge of the geometry of the probe apex. However, the use of well-defined geometry of the probes did not change the observed behavior of the modulus.^{38,53,54} Viscoelastic properties of materials and creep were also proposed to be a possible reason for the skin effect in the Oliver–Pharr method.^{22,24,37,45,55} Furthermore, the skin-effect was attributed to exceeding the elastic limit⁴⁰ and the use of incorrect projection area of the contact.^{33,56}

In the present work, we used AFM to study the skin effect by doing indentation of various polymers with different probes, processing the data through different models, and comparing the derived moduli with the bulk values measured for exactly the same polymers. Three different polymers of the bulk rigidity of 0.6–0.7 GPa (polyurethanes) and ~2.8 GPa (polystyrene) were studied with the AFM probes of well-defined spherical geometry (radii of the apex were 22, 810, and 1030 nm). The bulk moduli were defined for each sample material by using a dynamical mechanical analyzer (DMA). The

force-indentation curves obtained were processed with Oliver–Pharr, Hertz, JKR, and DMT models. We found that the skin effect disappeared when using the dull probes (of 810 and 1030 nm radii of curvature) and processing the force-indentation data with either of the adhesion models (JKR or DMT). Furthermore, we observed the values of the rigidity modulus that were very close to the bulk moduli when the indentations were as small as 2–3 nm. Finally, the observed values of the moduli were independent of the indentation depth, which is necessary (although not sufficient) condition of validity the models used. This suggests that the skin-effect can originate in both the nonlinearity of stress–strain relation (occurs when using too sharp probes) and the probe-surface adhesion that is not taken into account in some models (e.g., Oliver–Pharr and Hertz models).

EXPERIMENTAL DETAILS

Polymeric Samples. To prepare for polyurethane samples for the AFM study, two kinds of polyurethane pads JR111 and OXP4000 (Rohm and Haas EM, DE) were used. Small coupons of the pads were extracted from samples prepared by casting of polyurethane (during thermosetting) on a highly polished surface of a hard-drive disk. This brings nanoscale smoothness of the surface. Polystyrene samples were cut out of a crystal-grade polystyrene Petri dish (BD Falcon). Before the measurements, all samples were washed with a high purity ethanol (Sigma-Aldrich) and ultrapure water (Millipore, Inc.), and then dried under nitrogen. The AFM samples had the area of 7 × 7 mm² and 0.5–1.2 mm thickness. The samples were mounted on a metallic coin with a small amount of epoxy adhesive. The samples for the DMA study had the length, width, and thickness of 17.5, 10, and 0.5–1.2 mm, respectively.

DMA. The macroscopic (hereafter, bulk) rigidity moduli were determined using the TA Instruments Q800 Dynamic Mechanical Analyzer (DMA). A standard 17.5 mm single cantilever sample holder was used for all measurements. The measurements were performed under controlled force/strain rate for the static mode of operation. To determine the static bulk modulus, a simple quasistatic loading mode was used. The sample, clamped at both sides inside the single cantilever holder, was flexed at one end (so-called cantilever bending mode). The static modulus was calculated from the slope of the stress/strain curve. This study was conducted at room temperature (22–24 °C) using the maximum force of 18 N. The bulk values of the Young’s modulus were calculated using the strain less than 0.1% (as recommended by the manufacturer).

To match the measurement speed with the AFM indentation experiments, we additionally measured the moduli in the multistress/strain mode (using the same clamp setup). In this mode, the cycling

loading was applied to the sample at the rate of 0.8 Hz and the maximum load force of 0.10 N (which resulted in the amplitude of the flexible end of the clamp of $\sim 20 \mu\text{m}$).

Atomic Force Microscopy (AFM). Dimension 3100 (Bruker Nano/Veeco, Inc., CA) AFM with Nanoscope V controller and Nanoscope 7.3 software was used to record the force–indentation curves and acquire maps of the surface topography. In both cases a standard cantilever holder for operation in air was used. Force–indentation curves were recorded at the indentation rates of 800 nm/s (0.8 Hz ramp rate and 500 nm Z ramp size). The spring constant of the cantilever was measured using both thermal tune method⁵⁸ and the reference cantilever method.^{59,60} When using the latter method, several measurements were done as a function of the position on the reference cantilever to minimize the error of calculation of the unknown spring constant.^{61,62} The spring constant of the cantilevers used in this work ranged in 35–45 N/m. The sensitivity of the AFM photodiode was calibrated in each experiment against a clean silicon wafer. Sets of indentation curves with 20 load levels ranging from 150 nN to 6 μN were collected at three different areas for each sample–probe combination.

All AFM indentation measurements were performed using either RTESP AFM probes (Bruker Nano/Veeco, Inc.) or specially prepared hemispherical dull probes, see the below. The radius and shape of the RTESP AFM probes (hereafter, sharp probes) were evaluated by imaging a standard TipCheck sample (TIP001, Aurora NanoDevices, Canada). The shape and area of sharp probes were reconstructed using TipCheck-sample method (built-in option of Bruker Nano/Veeco, Inc. AFM software). The hemispherical dull probes (hereafter, dull probes) were made by using RTESP probes annealed in air at 1200 °C for 1–5 h.⁶³ Figure 1 shows an SEM image of such probes. The shape of the dull probes was found by imaging a reversed grid sample (TGT1, NT-NGT, Russia and TGT01, Micromash, Inc., Estonia). The dull probes used in this work have the shape close to an ideal spherical shape with the radii of either 810 or 1030 nm. All probes were measured twice, after the first indent on the polymer surface with the maximal load, and after all measurements.

Rigidity Models Used. To calculate the rigidity modulus, the measured force–indentation curves were processed with the help of the Hertz, DMT, JKR, and Oliver–Pharr models. The former three models deal with a spherical indenter. The latter model can work with the indenter of almost arbitrarily geometry. In the case of the Hertz model, the force–indentation curves were fitted by followed equation:

$$F_L(i) = \frac{4}{3} E^* \sqrt{R^*} i^{3/2} \quad (1)$$

where F_L is the load force, E^* is reduced Young's modulus: $E^* = E/(1-\nu^2)$, ν is the Poisson ratio, R^* is the reduced radius $1/R^* = 1/R_{\text{indenter}} + 1/R_{\text{surface}}$ and i is the indentation depth.

To take in to account adhesive interactions between a probe and surface, the DMT and JKR models were used. The DMT model uses eq 1 with an additional term related to adhesion (more precisely, the force at the point of “pull-off” of the AFM probe, or pull-off force for short) $F_{\text{pull-off}}$:

$$F_L(i) = \frac{4}{3} E^* \sqrt{R^*} i^{3/2} + F_{\text{pull-off}} \quad (2)$$

The pull-off force can easily be found from the force indentation curves.

The JKR model does not have explicit solution for $F_L(i)$. To fit experimental force–indentation curves, the followed parametric fitting was used:

$$i(a) = \frac{a^2}{R^*} - \sqrt{\frac{2\pi a w_{\text{adh}}}{E^*}} \quad (3)$$

$$F_L(a) = \frac{4E^* a^3}{3R^*} - 2\sqrt{2\pi E^* w_{\text{adh}} a^3} \quad (4)$$

where parameter a is the radius of contact, w_{adh} is the adhesion energy (per unit area) of interaction of two flat interfaces made of the

materials of the AFM probe and sample. It can be calculated by using the following equation:

$$w_{\text{adh}} = -2/3(F_{\text{pull-off}}/\pi R^*) \quad (4a)$$

In the case of a probe with arbitrary (but known) geometry, the Oliver–Pharr model is utilized.³³ In the first step of this model, the unloading part of the force–indentation curve is fitted with the help of a power law:

$$F_L(i) = A(i - i_f)^m \quad (5)$$

where A and m are the fitting parameters and i_f is the unloading depth corresponding to zero force when unloading.

In the next step, the contact stiffness S at the maximum load is calculated:

$$S = Am(i_{\text{max}} - i_f)^{m-1} \quad (6)$$

where i_{max} is the indentation at the maximum load.

The indentation depth i_c is calculated using the following formula:

$$i_c = i_{\text{max}} - \varepsilon \frac{F_{L\text{max}}}{S} \quad (7)$$

where $F_{L\text{max}}$ is the maximum load force, ε is an empirical constant equal to 0.75 in the case of a spherical indenter and 0.727 in the case of a sharp indenter.⁶⁴

Finally, the rigidity modulus is found by using the following formula:

$$E = \frac{1}{2\beta} (1 - \nu^2) S \frac{\sqrt{\pi}}{\sqrt{A(i_c)}} \quad (8)$$

Here $A(i_c)$ is the contact area at the indentation depth i_c , and β is an empirical correction factor ($\beta = 1.034$).⁶⁴

The maximum vertical compressive stress σ_{max} are reached at the center of the contact circle at the maximal load, F_{max} in the sample indented with a spherical probe (Hertz and DMT models) is found using the following equation:^{50,65}

$$\sigma_{\text{max spherical}} = \frac{3}{2} \frac{F_{\text{max}}}{\pi a^2} \quad (9)$$

The maximal shear stress calculated for a sharp probe is^{50,65}

$$\sigma_{\text{max conical shear}} = \frac{H}{2(1 + \alpha)} \quad (10)$$

Here a is the contact radius, α is the cone semiangle, $H = F_{\text{max}}/A(i_c)$, and F_{max} is either the load force in the Hertz model or the sum of the load and pull-off force in the DMT model.

In the case of JKR model, the maximum vertical compressive stress was calculated as follows:⁶⁵

$$\sigma_{\text{max}} = \frac{3}{2} \frac{F_{L\text{max}}}{\pi a^2} + 2 \frac{F_{\text{pull-off}} + \sqrt{F_{L\text{max}} F_{\text{pull-off}} + F_{\text{pull-off}}^2}}{\pi a^2} \quad (11)$$

The contact diameter is an important value that can be refereed as the lateral resolution of the indentation method. In the case of the Oliver–Pharr model, the contact diameter is an effective diameter of a circle which area is equal to the area of the probe at the height (calculated from the apex) equal to the contact depth. (It should be noted that the area at a particular contact depth is found directly when characterizing the probe.) For the other three models, the contact diameter d can be calculated though the following equations:

$$d = 2a = 2\sqrt[3]{\frac{3F_{L\text{max}} R^*}{4E^*}}, \quad \text{in the case of the Hertz model} \quad (12)$$

$$d = 2a = 2\sqrt[3]{\frac{3(F_{L\text{max}} + F_{\text{pull-off}}) R^*}{4E^*}} \quad \text{in the case of the DMT model} \quad (13)$$

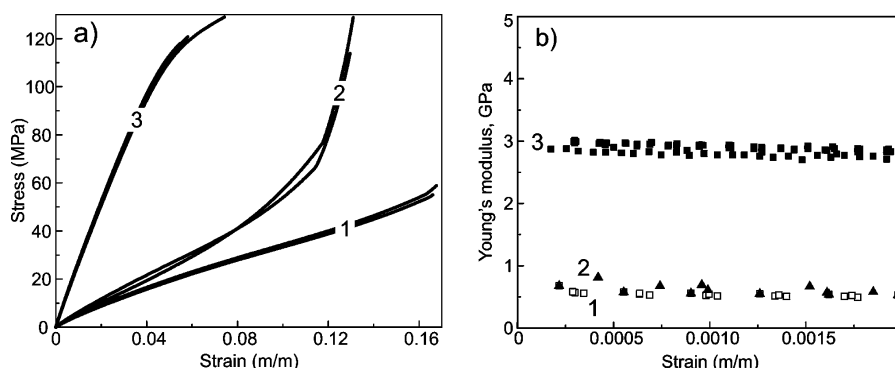


Figure 2. Results of the DMA analysis: (a) stress–strain curves for JR111 (1, open squares), OXP4000 (2, triangles), and polystyrene (3, black squares); (b) rigidity modulus as a function of strain.

$$d = 2a = 2\sqrt[3]{\frac{3R^*}{4E^*}(F_{L\max} + 2F_{\text{pull-off}} + \sqrt{4F_{L\max}F_{\text{pull-off}} + 4F_{\text{pull-off}}^2})}$$

in the case of the JKR model (14)

RESULTS AND DISCUSSION

DMA Bulk Moduli. To understand the nature of the skin effect (the dependence of the rigidity modulus on the indentation depth near the sample surface), it is useful to know the bulk moduli of the polymers used in the study. It will help to understand when the bulk modulus is reached in the nanoindentation experiments.

The results of the DMA measurements are shown in Figure 2. Figure 2a shows representative stress–strain curves for JR111, OXP4000 polyurethane and polystyrene samples. To avoid errors coming from plastic deformations, freshly cut samples were used in each single measurement. All samples showed close-to-linear behavior in the region of small strains and stresses, Figure 2b. A strong deviation from linearity is seen for stresses >50 MPa for polyurethane pads and >110 MPa for polystyrene sample.

The bulk values of the moduli, which were measured *quasistatically* for the small penetrations shown in Figure 2b, were (0.54 ± 0.04) GPa for JR111, (0.70 ± 0.20) GPa for OXP4000 and (2.87 ± 0.08) GPa for polystyrene. To match the speed of indentation in the AFM indentation experiments, we further measured the bulk moduli using the DMA deformation rate of 0.8 Hz (multi-stress/strain DMA mode). The values of the moduli obtained in this mode were found to be insignificantly different: (0.65 ± 0.06) GPa for JR111, (0.68 ± 0.07) GPa for OXP, and (2.8 ± 0.1) GPa for polystyrene. We will use the latter values as the bulk moduli of the polymers of study.

AFM Indentation: The Sharp Probe Case. A sharp indentation probe was used to collect the force–indentation curves with the indentation depth up to ~ 90 nm (corresponded to the maximum force of ~ 5 μ N used in all experiments described in this work). The deflection sensitivity of this AFM cantilever was linear up to this limit (this can be seen by measuring the compliance region on a rigid substrate). The curvature radius of the apex was 22 ± 8 nm (the error is one standard deviation of five independent measurements). The shape of the probe in such indentations was far from being spherical. Therefore, Oliver–Pharr model was used to derive the rigidity modulus. Hereafter, the Poisson ratios for all materials were taken from the literature.^{66–68} (0.38 for polystyrene and 0.4 for polyurethane)

Figure 3 shows the rigidity modulus as a function of indentation (i_c) given by eq 8. The maximum shear stress (eq

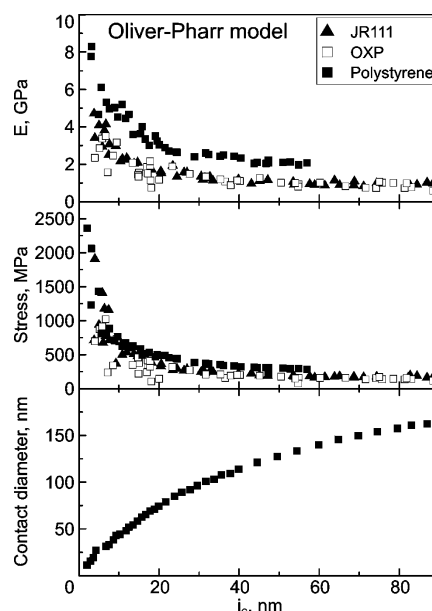


Figure 3. Rigidity modulus, maximum shear stress, and indentation contact diameter as functions of the indentation depth. All values were calculated using the Oliver–Pharr model by processing the force–indentation curves collected with the AFM sharp probe. The contact diameter is an effective one of a circle that has the same area as the area of the probe at the height (calculated from the apex) equal to the contact depth (the area at the particular contact depth is found directly when characterizing the probe).

10) and the size of the tip–sample contact as functions of the indentation depth are also shown to estimate possible level of the stress–strain nonlinearity and the size of the indent (aka the lateral spatial resolution of this method). The contact diameter here is an effective one of a circle that has the same area as the area of the probe at the height (calculated from the apex) equal to the contact depth (the area at the particular contact depth is found directly when characterizing the probe).

As seen from Figure 3, the value of the rigidity modulus increases at small penetration for all three polymers of study. This is what we described in the Introduction as the skin effect. When the indentation is greater than ~ 30 nm, the values of the rigidity modulus become relatively constant (although being still slightly decreasing). The “plateau averaged” values are $(0.99 \pm$

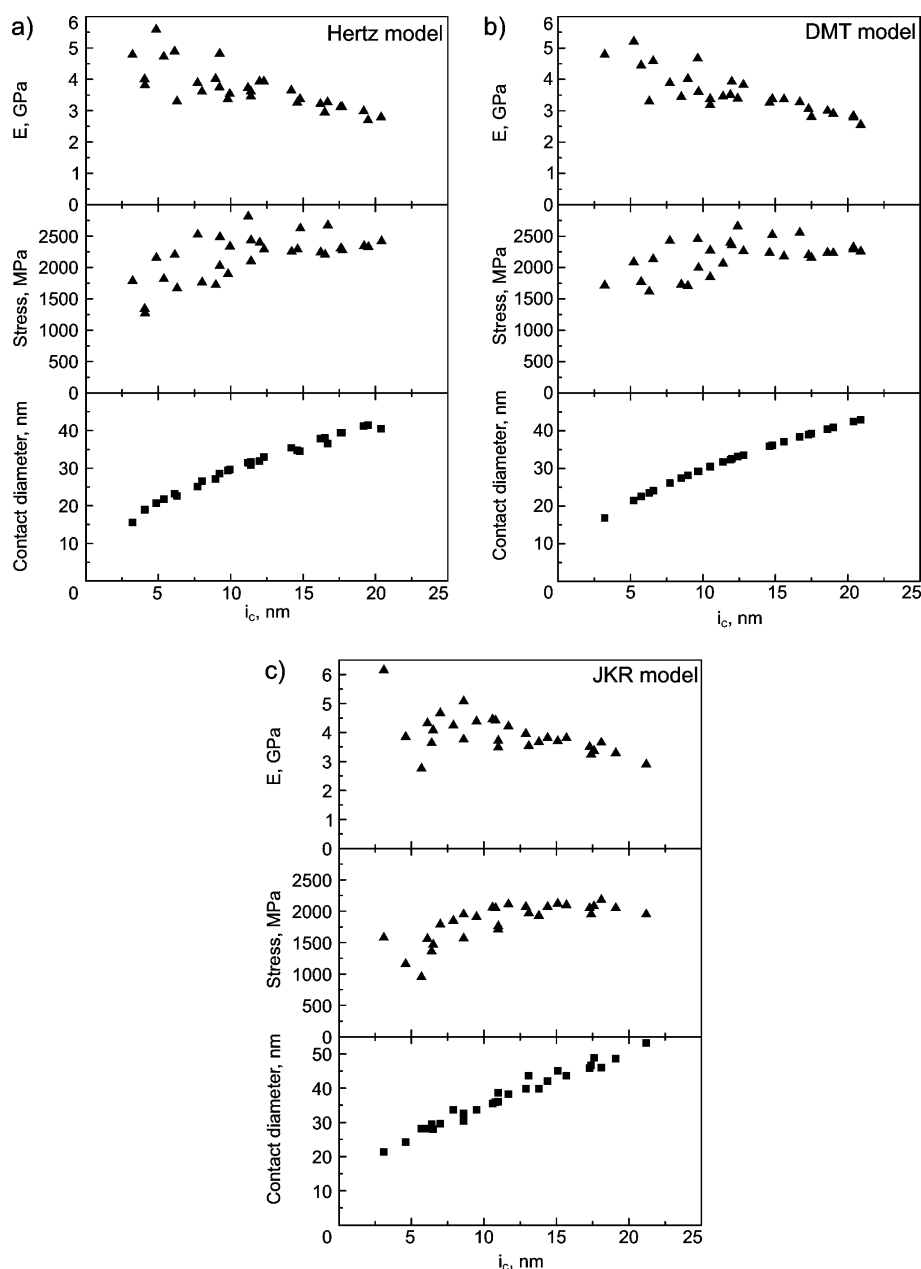


Figure 4. Results of processing of the force–indentation curves collected with the AFM sharp probe. The results are shown for (a) Hertz, (b) DMT, and (c) JKR models. The rigidity modulus, maximum stress, and the contact diameter are shown as functions of the indentation depth.

0.13) GPa for JR111, (0.94 ± 0.18) GPa for OXP, and (2.2 ± 0.2) GPa for the polystyrene sample. At the maximum indentations, the moduli reach values of ~ 0.8 GPa for both polyurethane samples and ~ 2 GPa for the polystyrene sample. It should be noted that these values still deviate from the DMA bulk values. Specifically, the value of the modulus at the plateau is 152% of the bulk value for JR111, 138% for OXP, and 80% for the polystyrene sample.

The skin effect unlikely comes from the changes in the polymer structure near surface, because the samples were prepared fresh. Moreover, both freshly prepared samples and the ones tested after some “aging” time (a few days stored at a closed container) showed similar results. As was mentioned, the model used might be the reason for the observed skin effect. Another straightforward reason is the nonlinearity of the

stress–strain relation for the small indentations, which is clearly seen in Figure 2.

Let us repeat similar calculations of the values shown in Figure 3 using the other models. Because the probe can be approximated by a sphere for the indentations smaller than the radius of the apex (22 nm), it is possible to use the Hertz, DMT, and JKR models. Figure 4a–c) shows the results of processing the indentation data for JR111 sample through these models. One can see that the rigidity modulus is decreasing with increasing the indentation depth. The values of the rigidity moduli (calculated by using eqs 1–4) are substantially higher than the bulk values, in particular in the cases of Hertz and DMT models. Although the value of the modulus derived in the JKR model is smaller in comparison with the other models, it is still well above the bulk values. Comparing the stresses (eq 9–11) with the linear stress–strain limits, one can see that the

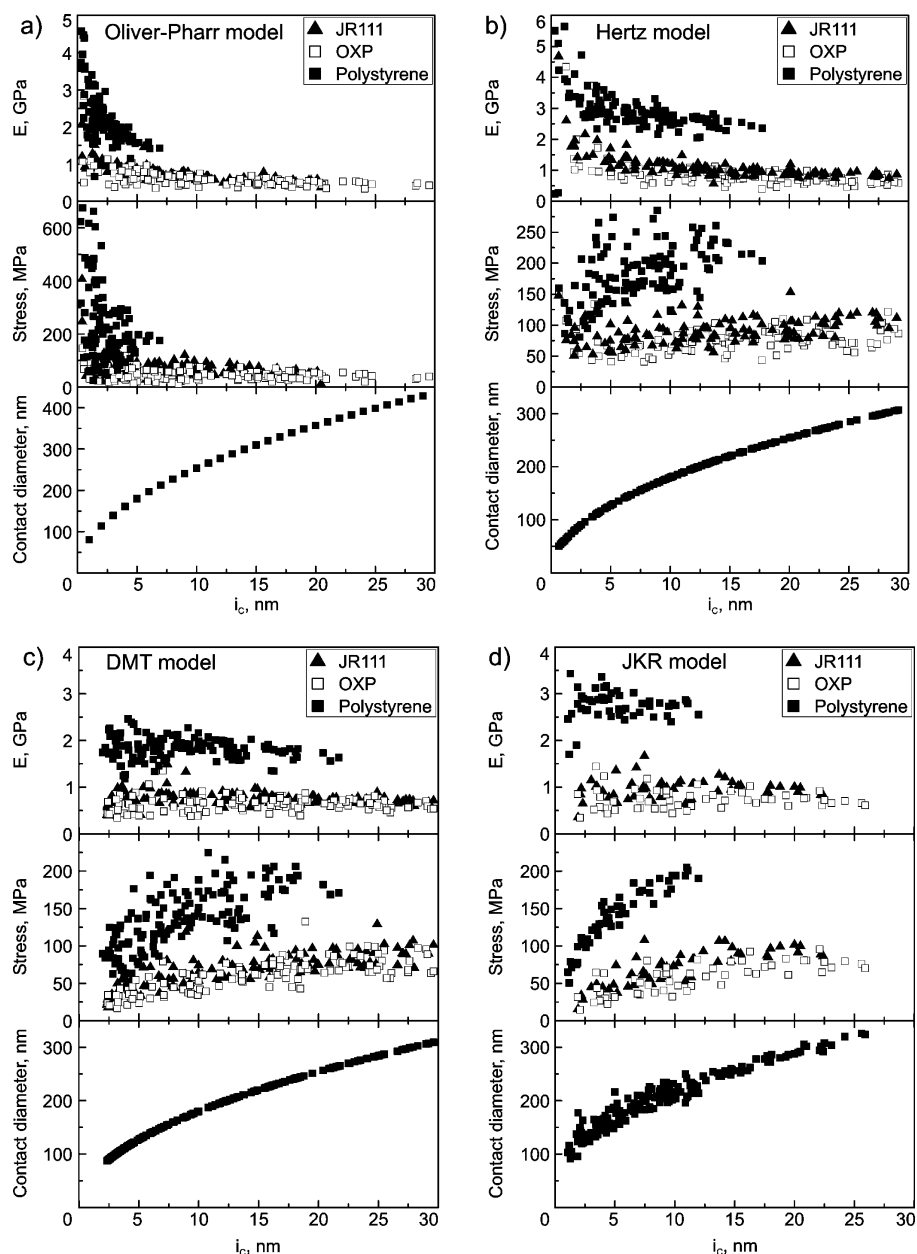


Figure 5. Results of processing of the force–indentation curves collected with the AFM dull probe. The results are shown for (a) Oliver–Pharr, (b) Hertz, (c) DMT, and (d) JKR models. The rigidity modulus, maximum stress, and the contact diameter are shown as functions of the indentation depth.

stresses obtained are in the strong nonlinear range for all three models. The other polymers of study show similar high stresses of the nonlinear regime (not shown).

On the basis of these results, it is conceivable to suggest that the skin effect may be a result of high nonlinearity of the stress–strain relation. This nonlinearity is clearly seen when comparing the maximum stress produced by the probe (Figures 3 and 4(a–c)) and the maximum stress level where nonlinearity is small, Figure 2a (50 MPa for polyurethane and for 110 MPa polystyrene samples). The values of the stress are clearly in the nonlinear regime in all models. In the case of the Hertz, DMT, and JKR models, the maximum stress reaches ~ 2500 MPa for JR111 polymer in the Hertz, DMT models and ~ 2100 MPa in the JKR model. This is well above the linear regime for this sample (< 50 MPa).

AFM indentation: the dull probe case. To eliminate the problem of nonlinearity of the stress–strain response, we used dull indentation probes. Close-to-spherical probes were used with the radius of curvature of either 810 ± 80 nm or 1030 ± 95 nm (the error is one standard deviation of five independent measurements of the radii). The maximum indentation was ~ 30 nm, which is less than the indentations attained with the sharp RTESP probes because of the same maximum force of $5 \mu\text{N}$ used in this work. The large spherical shape of the probes allowed using the Hertz, DMT and JKR models for the entire indentation range.

The values of the rigidity moduli, the maximum stresses, and the diameters of contact as functions of the indentation depth were derived using the Oliver–Pharr, Hertz, DMT, and JKR models as described in the Experimental Details. The values of the adhesion energy w_{adh} used for the JKR calculation were

found using equation (4a) for every force curve. These values do not depend on the indentation depth if no plastic deformation is observed. The values of the adhesion energy measured with both dull probes were indeed radius and penetration independent, and resulted in $w_{adh} = 0.035 \pm 0.015$ J/m² (the same value for both polyurethanes) and $w_{adh} = 0.038 \pm 0.005$ J/m² (polystyrene). The larger standard deviation of the adhesion energy for polyurethanes compared to polystyrene is expected because of high heterogeneity of the polyurethane. (We did not present similar data when using the sharp probe, because it would be rather speculative to evaluate the adhesion energy since the true shape of the contact at the pull-off is not well-known.)

Figure 5 shows the rigidity moduli, the maximum stresses in the vicinity of the probe, and the diameters of contact as a function of the indentation depth. For the case of the Oliver–Pharr and Hertz models, one can see that the elastic modulus still decreases with the indentation depth for all polymers of study. In both models (except the case of Oliver–Pharr model applied to the polystyrene sample), the rigidity moduli reach plateau at some indentation depth. The values of the plateau modulus (indentation depth >10 nm) approach (0.60 ± 0.06) GPa (Oliver–Pharr) and (0.94 ± 0.14) GPa (Hertz) for the JR111 sample, (0.52 ± 0.09) GPa (Oliver–Pharr) and (0.72 ± 0.18) GPa (Hertz) for the OXP sample, and ~ 1.55 GPa (Oliver–Pharr; no plateau was reached) and (2.58 ± 0.22) GPa (Hertz) for polystyrene samples. One can see that the plateau values are relatively close to the bulk ones. However, neither of these two models could still correctly provide the value of the rigidity modulus at small indentation depth.

In the case of two other DMT and JKR models, which take adhesion into account, there is virtually no skin effect seen in Figure 5c,d. Rigidity modulus of polystyrene obtained using DMT method show average value of (1.82 ± 0.28) GPa, Figure 5c. It is 35% smaller than the bulk value of the rigidity modulus. At the same time, the JKR model (Figure 5d) gives the modulus of (2.75 ± 0.30) GPa which is exactly the bulk value within the error. In the case of OXP polyurethane sample, both methods give rigidity moduli close to the DMA bulk moduli. The average values are (0.63 ± 0.15) GPa (8% less than the bulk values) for the DMT model, and (0.74 ± 0.21) GPa (8% more than bulk) for the JKR models, respectively. However, in the case of JR111 samples, the differences are larger, 14% higher than the bulk value for DMT, and 47% for JKR models.

Comparing the obtained rigidity moduli, the maximum stresses, and the corresponding bulk values, we can conclude that the skin effect virtually disappears when using the adhesion models, JKR and DMT. Moreover, the values of the moduli derived in the adhesion models are better match the bulk values derived with DMA method than the values obtained with a sharp probe. This is presumably the result of linearity of the stress–strain relation, which is clearly seen when comparing the maximum stress vertical compressive produced by the dull probe with the threshold of nonlinearity (50 MPa for polyurethane and for 110 MPa polystyrene samples, Figure 2a).

Comparison of the Indentations Done with the Dull and Sharp Probes. Besides the broken linearity of the stress–stress relation when using the sharp probe, there are some important differences in the measurements done when using the sharp and dull probes. A hysteresis was observed in the trace–retrace force–indentation curves when using the sharp probe for all measured loads. We do not see the hysteresis when using the dull probes for the load force less than 3–5

μ N. Figure 6 shows the typical indentation curves collected with the sharp and dull probes. One can see that the trace and

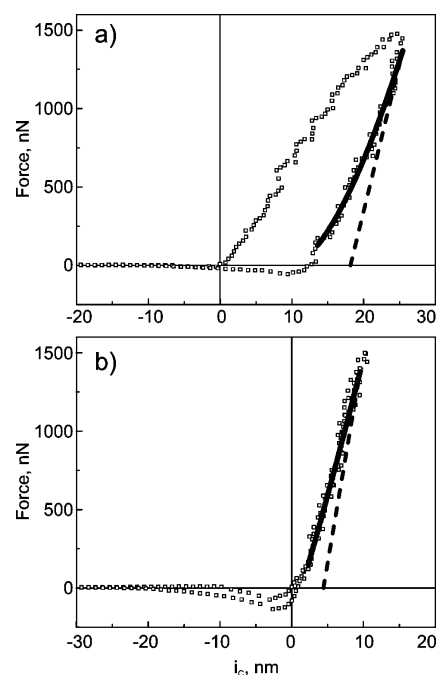


Figure 6. Representative indentation curves when using (a) sharp and (b) dull indentation probes (JR111 example).

retrace curves almost coincide for the dull probe, while there is a clear hysteresis when the sharp probe is used. Since we performed indentations in a relatively slow deformation speed, the presence of the hysteresis can be explained by the occurrence of plastic deformations. Therefore, it is important to use the retracted part of the curve to derive the modulus of rigidity in the case of the sharp probe. For the dull probe, both curves give essentially the same results.

Another important difference of the indentations is in the maximum stress that is attained with the sharp and dull probes. Since the contact area is substantially smaller for the sharp probe, it is plausible to expect the maximum stress will also be substantially higher for sharp probes. This is directly confirmed by calculation of maximal stress shown in Figures 3, 4, and 5. One can see that the stress produced by a sharp probe is an order of magnitude higher than stress under dull probe (at the indentation depth <25 nm). Note that all figures show the maximum possible stress which can be substantially higher than the mean stress around the probe. The large hysteresis of Figure 6a is another confirmation of high stress in the case of indentation with sharp probe (which exceeds the limit of the yield stress).

The presence of plastic deformations is directly confirmed by the AFM imaging of the pre- and post-indentation images of the surface. Figure 7 shows an example of such images for JR111 polyurethane sample after indenting with the sharp probe. The indentations shown were performed with the load force of 1–5 μ N. One can see the well-marked plastic dents for the entire range of the load forces used. A similar couple of images are shown in Figure 8 for the case of the dull probe when the load force ranges between 1 and 5 μ N. One can see that the dull probe did not produce any noticeable dents in the sample surface (to make a mark point, a load force of 10 μ N

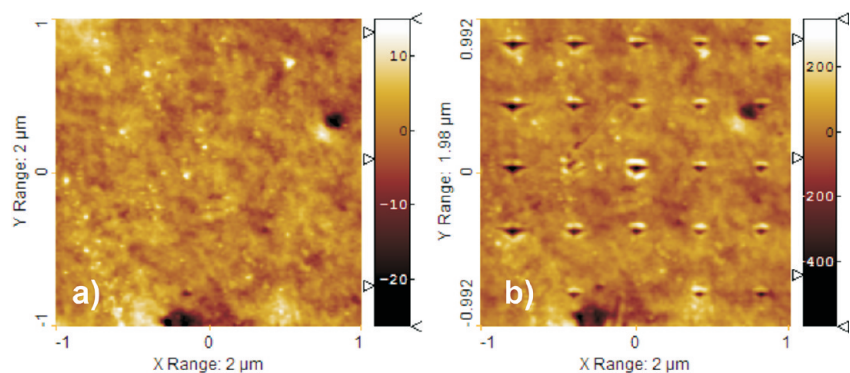


Figure 7. Surface topography of JR111 sample: (a) before and (b) after indentations performed with the sharp AFM probe. The indentations were done with 1–5 μN load forces (which increase from the right to the left in each row).

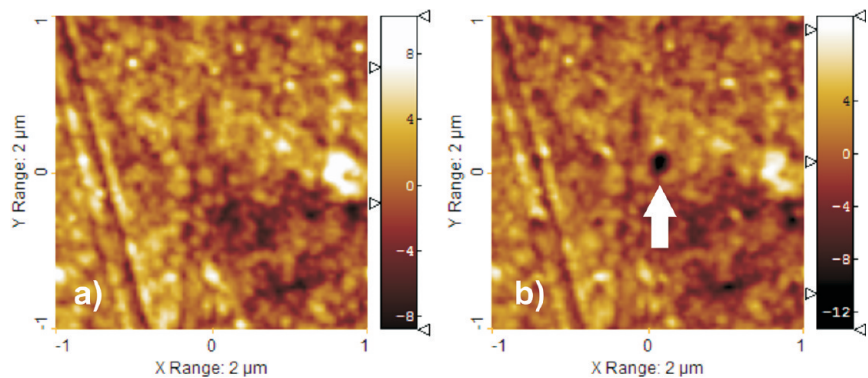


Figure 8. Surface topography of JR111 sample: (a) before, and (b) after indentations performed with the dull AFM probe. The indentations were done with 1–5 μN load forces. The arrow in panel b highlights the indentation mark made with a high load force of 10 μN .

Table 1. Summary of the Rigidity Moduli Derived When Using Various Models and AFM Indentation Probes^a

	JR111, GPa	OXF, GPa	PS, GPa	max stress, MPa	contact diameter, nm	depth, nm	skin effect
macro DMA	0.65 ± 0.06	0.68 ± 0.07	2.8 ± 0.1	~ 0.8	$\sim 5 \times 10^6$	n/a	n/a
AFM- sharp probe: Oliver	0.99 ± 0.13	0.94 ± 0.18	2.23 ± 0.21	~ 300	>10	>30	strong
AFM- sharp probe: Hertz	4.0/2.9	—	—	2300/2450	29/41	10/20	strong
AFM- sharp probe: DMT	4.0/2.8	—	—	2100/2250	29/41	10/20	strong
AFM- sharp probe: JKR	3.9/3.0	—	—	1800/2000	34/51	10/20	strong
AFM- dull probe: Oliver	0.6 ± 0.06	0.52 ± 0.09	<1.6	50–100	180–250	>10	weak
AFM- dull probe: Hertz	0.94 ± 0.14	0.72 ± 0.18	2.58 ± 0.22	75–200	>180	>10	weak
AFM- dull probe: DMT	0.74 ± 0.14	0.63 ± 0.15	1.82 ± 0.28	50–75	100	~ 2	no
AFM- dull probe: JKR	0.96 ± 0.21	0.74 ± 0.21	2.75 ± 0.30	40–125	120	~ 2	no

^aThe rigidity moduli shown are the plateau values (when it weakly depends on indentation). If plateau was not reached, the modulus value is given as inequality. The maximum contact stresses, the contact diameter, and indentation depth correspond to the rigidity modulus presented in the table.

was used; the corresponding dent is seen at the middle of Figure 8b as highlighted by an arrow).

The last important difference between the sharp and dull probes is the dissimilarity in the pull-off force. In the case of purely elastic deformation (and ideally smooth probe), the pull-off force is proportional to the radius of curvature of the probe.⁶⁹ However, instead of the expected ratio of the pull-off forces to be $>36\times$ for the dull probe compared to the sharp one, in our experiments the pull-off force is only $2.4\times$ higher in average ($\sim 2.9\times$ in the example shown in Figure 6). Since the chemistry of both types of probes is similar, such a small ratio can conceivably be explained by the presence of plastic deformation. Obviously, the area of contact between the probe and surface is larger when plastic deformations are present. Since the pull-off force is proportional to the area of contact at the moment of disconnection, the pull-off force is

noticeably larger for the sharp probe compared to no-plastic deformation case.

Comparing Results and Validity of the Models Used.

The results described so far are summarized in Table 1. The rigidity moduli shown are the plateau values (when it weakly depends on indentation). If plateau was not reached, the modulus value is given as inequality. The maximum stresses, the contact diameters, and indentation depths at which the rigidity modulus was reached are collected in the table.

One can see from the table that the rigidity modulus can be substantially different when using indenters of different shapes even for the same sample and model. The rigidity moduli are close to the bulk values only in one case, when using the dull probe and adhesion (DMT or JKR) model. In addition, there is no skin effect observed in that case. Let us discuss the possible reasons for such observations.

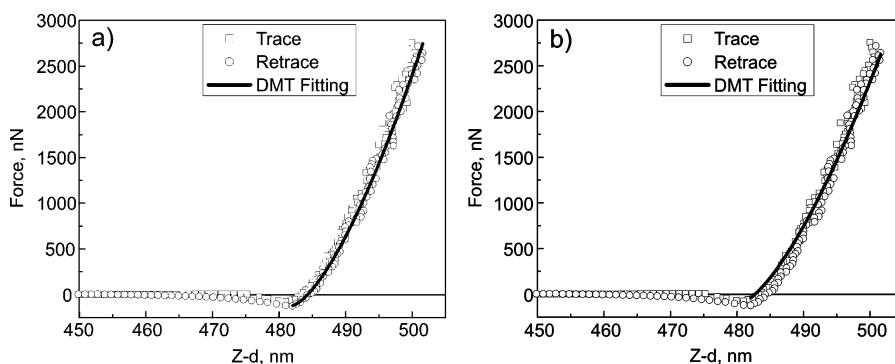


Figure 9. Representative indentation curve measured with dull 810 nm probe. Open squares and circles represent approaching and retracting of force-indentation curve. Solid line is the fitting done with the DMT model when the point of the probe-sample contact (a) was chosen as free fitting parameter (to minimize the fitting error) or (b) was manually put equal to 480 nm.

It is known that the Oliver–Pharr model may produce incorrect results for viscoelastic materials.^{33,37,38,45} In particular, the modulus dependence on the indentation depth, which is different for different probe shape, has been unresolved problem in that model. It is also worth noting that the Oliver–Pharr model considers the elastic response in the presence of plastic deformations to be the same as in the case of purely elastic deformation. This can be incorrect for materials like polymers. Finally, the Oliver–Pharr model does not take into account the probe-sample adhesion.

When using the dull probe, plastic deformations are absent as was shown above. Furthermore, the use of the dull spherical probe is advantageous because it allows a) working in regime of small stresses (in the linear stress–strain regime), and b) taking into account adhesion (DMT or JKR models). Therefore, it is not surprising to see in Table 1 that the rigidity moduli are closer to the bulk values in the case of the dull probe.

Let us finally analyze the difference of the results obtained with help of the DMT and JKR models. As seen from Table 1, the DMT model is in a good agreement with the bulk values for polyurethane samples, but it gives much smaller modulus for the polystyrene sample. In contrast, the JKR model determines the rigidity modulus more accurately for the polystyrene sample. At the same time, this model leads to slightly overestimated moduli values for polyurethane samples, though the deviation from the bulk moduli is within one standard deviation. The choice between the JKR and DMT models can be done based on the use of the Maugis parameter α ,^{51,65} which is a dimensionless parameter ranging between 0 and 1. α close to 1 justifies the use of the JKR model, whereas α close to 0 points to the use of the DMT model. The Maugis parameter α relates to the Tabor parameter μ_T ⁷⁰ as follows:⁵¹

$$\alpha = -\frac{50}{51} (e^{-250\lambda/231} - 1) \quad (15)$$

where $\lambda = 1.157(w_{adh}^2 R^*/E^* D_0^3)^{1/3}$,^{51,65} w_{adh} is the adhesive energy per unit area, R^* is the reduced radius ($1/R^* = 1/R_1 + 1/R_2$), $E^* = E/(1 - \nu^2)$ is the reduced Young's modulus, and ν is the Poisson ratio. D_0 is the interatomic distance between the atoms of probe and sample at contact. It can be estimated using equation for the pure van der Waals adhesion:⁶⁹ $D_0 = (A_H/(24\pi w_{adh}))^{1/2}$, where the w_{adh} is the adhesion energy, A_H is the Hamaker constant. $A_H = (6-7) \times 10^{-20}$ J for polyurethane–vacuum–silica (this constant is unknown for the specific polyurethane used in this work, but we can assume this value because it is rather similar for most of polyurethanes), and $A_H =$

6.5×10^{-20} J is for polystyrene–vacuum–silica.⁶⁵ This gives $D_0 = 0.16 \pm 0.03$ nm for the case of polyurethane–vacuum–silica and $D_0 = 0.15 \pm 0.01$ nm for the polystyrene–vacuum–silica interaction. The estimated Maugis parameters for both dull probes are 0.98 for polyurethane samples, and 0.96 for the polystyrene sample. Thus, the use of the JKR model is more appropriate for all samples in this work.

Analysis of Possible Errors. To exclude coincidental agreement of the rigidity moduli for the surface and bulk, we need to analyze possible errors in calculation of the moduli obtained in this work. The main source of the measurement errors in the AFM experiment typically originates from inaccurate determination of the size and shape of the indenter probe,⁴⁵ not well-known Poisson ratio, uncertainty in the determination of the point of contact, the error in measuring the spring constant of the AFM cantilever, from the surface and probe roughness, scanner and sample creep, AFM photodetector nonlinearity.^{31,71–73} In our work, we exclude AFM photodetector nonlinearity and scanner creep by using the close-loop scanner and calibrating the photodetector as described by the manufacturer. The roughness of annealed or fresh sharp probes is also very small.⁷⁴ We analyze the influence of the other errors on the rigidity modulus calculated here.

Let us first analyze the error coming from inaccuracy in definition of the probe-sample contact point. Figure 9a shows a representative force-indentation curve used to derive the value of the rigidity modulus. As an example of the use of DMT model, the fitted curve predicted by the DMT model (eq 2) is well matched with the experimental points in the entire fitting range. In this fitting procedure, the point of contact was one of the fitting parameters, i.e., was chosen to minimize the fitting error (equals to 481.9 nm). However, in principle, it can be chosen manually by visual judgment. This situation is presented in Figure 9b, in which the fitting is done with the contact point that was manually chosen to be at 480.0 nm, which is look like the worst visual choice. One can see that it leads to a bigger discrepancy between the experimental points and fitting curve, in particular in the region of small forces. Obviously, it will result in a different value of the rigidity modulus. A similar analysis done on a representative set of the load-indentation curves shows that the uncertainty of definition of the rigidity modulus due to the different choice of the contact is $\sim 10\%$. It is not always true that the point of contact minimizing the fitting error is the best one. Because of the measurement noise, the best fitting does not always correspond to the true point of contact, and consequently the derived value of the rigidity

modulus can be biased. There were numerous attempts to find the true contact point. For example, some correction coefficients were added to find true point of contact to illuminate the depth dependence of the rigidity modulus in this way.⁷⁵ In other works, the problem of automatic AFM curve analysis and determination of the true point of contact was also discussed.^{72,73,76} To avoid the ambiguity of the correctness of defining the true point of contact, we treat this uncertainty in the definition the rigidity modulus as an error.

The error coming from the uncertainty of the spring constant of the AFM cantilever equals to the error of the rigidity modulus (because the rigidity modulus is generally proportional to the load force which is proportional to the spring constant). It is commonly accepted that the spring constant of the AFM cantilever can be measured with 10–20% error.^{59–63} This implies that we should expect 10–20% error in the definition of the rigidity modulus. It should be noted that this error, being the same multiplicative factor for all measured moduli, does not change the dependence of the modulus on the indentation depth.

The error of the modulus due to the uncertainty in the definition of the probe radius is a relatively small, mostly because of the use of high resolution AFM tip-check method to define the shape of the indenter. For example, the radii of the dull probes used in this work have the error of 10%. According to eqs 1–4, it results in an error of ~5% in the definition of the rigidity modulus.

Similar equations can be used to estimate the error due to the uncertainty in the Poisson ratio. If we vary the Poisson ratio between 0.4 and 0.5, which seems to be the maximum uncertainty for the Poisson ratio of our polymer reported in the literature,^{66–68} the error in the calculation of the rigidity modulus is ~10%.

As to the error coming from the creep effect of the sample, it was found that the polymer creep caused overestimation of the rigidity modulus up to ~30%.^{45,77} This is so far not sufficient to explain the much higher rigidity compared to the bulk observed for the case of the sharp probe. As to the dull probes, the creep effect can be neglected since we do not observe the hysteresis between load-unload force-indentation curves. To conclude, neither of these errors seems to be capable of explaining the skin effect, which is much stronger than the errors discussed here.

CONCLUSION

Here we investigated the dependence of the rigidity modulus on the indentation depth observed for supposed-to-be-homogeneous soft materials, a phenomenon we suggest to call the skin effect (to contrast with the indentation size effect observed for the rigid materials, metals, which presumably has a different nature). We studied the indentation with the help of atomic force microscopy (AFM). This allowed us controlling the load force with very high precision compared to the existing nanoindenters. Furthermore, we used the indenting probes of well-defined geometry (radii of ~22, 810, and 1030 nm). Three polymers of the bulk rigidity 0.6–0.7 GPa (polyurethanes) and 2.8 GPa (polystyrene) were used in this study. The bulk rigidity modulus was measured for these specific samples with the help of DMA setup.

The obtained force-indentation curves were processed through the Oliver–Pharr, Hertz, Johnson–Kendall–Roberts (JKR), and Derjaguin–Muller–Toporov (DMT) models. The latter two models take into account adhesion between the

probe and sample surface. We found that the skin effect virtually disappeared when using both dull (810 and 1030 nm) probes and processing the force-indentation curves through the model that takes into account the probe-sample adhesion (JKR or DMT). Analyzing the Maugis parameter, we concluded that JKR model was the appropriate one to use here. The obtained surface moduli were found to be rather close to the bulk values for polyurethanes, and be a perfect match the bulk value of polystyrene. Specifically, the values of the rigidity modulus were very close to the bulk values starting from the indentations as small as 2–3 nm. A small discrepancy (although within one standard deviation) observed for polyurethane samples might be explained by the excessive number of defects in the used polyurethane, which obviously give smaller macroscopic modulus of rigidity.

These results suggest that the skin-effect originates at both the nonlinearity of stress-strain relation (occurs when using sharp probes) and ignoring the probe-surface adhesion. In the other words, the indentation measurements give the correct value of the bulk modulus of rigidity for even small indentations without visible skin-effect if the measurements are done in the linear stress-strain regime and processed through a model that takes the probe-sample adhesion into account.

We expect that the methods described in this work can be used to measure the true modulus of rigidity at small indentations. This should be useful to study rigidity of thin films (small indentations could help to exclude the influence of the substrate on the mechanics of the film). Furthermore, the small indentation is associated with a smaller area of contact. This brings a higher lateral resolution in defining the rigidity modulus. This can be advantageous for the study of nanocomposite materials to avoid the averaging effect when doing the indentation with excessively large area of contact.

AUTHOR INFORMATION

Corresponding Author

*Mailing address: 8 Clarkson Ave., Clarkson University, Potsdam, NY 13699-5820. E-mail: isokolov@clarkson.edu. Telephone: 1-315-268-2375.

Notes

The authors declare no competing financial interest.

REFERENCES

- (1) Sahin, O.; Magonov, S.; Su, C.; Quate, C. F.; Solgaard, O. An atomic force microscope tip designed to measure time-varying nanomechanical forces. *Nat. Nanotechnol.* **2007**, *2* (8), 507–514.
- (2) Oliver, W. C. New nanoindentation and scanning probe tools and techniques. *Surf. Interfaces Nanostruct. Mater. Trends LIGA, Miniaturization, Nanoscale Mater.* **2004**, 299.
- (3) Asif, S. A. S.; Wahl, K. J.; Colton, R. J.; Warren, O. L. Quantitative imaging of nanoscale mechanical properties using hybrid nano-indentation and force modulation. *J. Appl. Phys.* **2001**, *90* (3), 1192–1200.
- (4) Ong, Q. K.; Sokolov, I.; Chechik, N.; James, D. AFM study of forces between polyurethane pads and ceria nanoparticles. *Abstracts of Papers, Part 2*; 229th National Meeting of the American Chemical Society: San Diego, CA, March 13–17, 2005; American Chemical Society, Washington DC, 2005, PMSE 56, U1111.
- (5) Sokolov, I.; Ong, Q. K.; Shodiev, H.; Chechik, N.; James, D.; Oliver, M. AFM study of forces between silica, silicon nitride and polyurethane pads. *J. Colloid Interface Sci.* **2006**, *300* (2), 475–481.
- (6) Wang, Y. L.; Liu, C.; Chang, S. T.; Tsai, M. S.; Feng, M. S.; Tseng, W. T. Chemical-mechanical polishing of low-dielectric-constant

- spin-on-glasses: film chemistries, slurry formulation and polish selectivity. *Thin Solid Films* **1997**, 308, 550–554.
- (7) Meyers, M. A.; Lin, A. Y.; Chen, P. Y.; Muiyco, J. Mechanical strength of abalone nacre: role of the soft organic layer. *J. Mech. Behavior Biomed. Mater.* **2008**, 1 (1), 76–85.
- (8) Lekka, M.; Laidler, P.; Gil, D.; Lekki, J.; Stachura, Z.; Hryniewicz, A. Z. Elasticity of normal and cancerous human bladder cells studied by scanning force microscopy. *Eur. Biophys. J.* **1999**, 28 (4), 312–316.
- (9) Cross, S. E.; Jin, Y. S.; Rao, J.; Gimzewski, J. K. Nanomechanical analysis of cells from cancer patients. *Nature Nanotechnol.* **2007**, 2 (12), 780–783.
- (10) Iyer, S.; Gaikwad, R. M.; Subba-Rao, V.; Woodworth, C. D.; Sokolov, I. AFM Detects Differences in the Surface Brush on Normal and Cancerous Cervical Cells. *Nature Nanotechnol.* **2009**, 4, 389–393.
- (11) Sokolov, I.; Iyer, S.; Subba-Rao, V.; Gaikwad, R. M.; Woodworth, C. D. Detection of surface brush on biological cells in vitro with atomic force microscopy. *Appl. Phys. Lett.* **2007**, 91, 023902-1–023902-3.
- (12) Suresh, S. Biomechanics and biophysics of cancer cells. *Acta Biomater.* **2007**, 3 (4), 413–438.
- (13) Sokolov, I.; Iyer, S.; Woodworth, C. D. Recover of Elasticity of Aged Human Epithelial Cells In-Vitro. *Nanomed.: Nanotechnol., Biol. Med. (Nanomed.)* **2006**, 2, 31–36.
- (14) Cheng, Y. T.; Cheng, C. M. Scaling, dimensional analysis, and indentation measurements. *Mater. Sci. Eng. R-Rep.* **2004**, 44 (4–5), 91–149.
- (15) VanLandingham, M. R. Review of instrumented indentation. *J. Res. Natl. Inst. Stand. Technol.* **2003**, 108 (4), 249–265.
- (16) Vlassak, J. J.; Nix, W. D. Measuring the Elastic Properties of Anisotropic Materials by Means of Indentation Experiments. *J. Mech. Phys. Solids* **1994**, 42 (8), 1223–1245.
- (17) Hodzic, A.; Kalyanasundaram, S.; Kim, J. K.; Lowe, A. E.; Stachurski, Z. H. Application of nano-indentation, nano-scratch and single fibre tests in investigation of interphases in composite materials. *Micron* **2001**, 32 (8), 765–775.
- (18) An, L.; Chan, H. M.; Padture, N. P.; Lawn, B. R. Damage-resistant alumina-based layer composites. *J. Mater. Res.* **1996**, 11 (1), 204–210.
- (19) Misra, A.; Hirth, J. P.; Hoagland, R. G. Length-scale-dependent deformation mechanisms in incoherent metallic multilayered composites. *Acta Mater.* **2005**, 53 (18), 4817–4824.
- (20) Volinsky, A. A.; Moody, N. R.; Gerberich, W. W. Interfacial toughness measurements for thin films on substrates. *Acta Mater.* **2002**, 50 (3), 441–466.
- (21) Gouldstone, A.; Koh, H. J.; Zeng, K. Y.; Giannakopoulos, A. E.; Suresh, S. Discrete and continuous deformation during nano-indentation of thin films. *Acta Mater.* **2000**, 48 (9), 2277–2295.
- (22) Domke, J.; Radmacher, M. Measuring the elastic properties of thin polymer films with the atomic force microscope. *Langmuir* **1998**, 14 (12), 3320–3325.
- (23) Godovsky, Y. K.; Magonov, S. N. Atomic force microscopy visualization of morphology and nanostructure of an ultrathin layer of polyethylene during melting and crystallization. *Langmuir* **2000**, 16 (7), 3549–3552.
- (24) Dimitriadis, E. K.; Horkay, F.; Maresca, J.; Kachar, B.; Chadwick, R. S. Determination of elastic moduli of thin layers of soft material using the atomic force microscope. *Biophys. J.* **2002**, 82 (5), 2798–2810.
- (25) Sokolov, I.; Subba-Rao, V.; Luck, L. A. Change in Rigidity in the Activated Form of the Glucose/ Galactose Receptor from E-coli: A Phenomenon That Will Be Key to the Development of Biosensors. *Biophys. J.* **2006**, 90, 1055–1063.
- (26) A-Hassan, E.; Heinz, W. F.; Antonik, M. D.; D'Costa, N. P.; Nageswaran, S.; Schoenenberger, C. A.; Hoh, J. H. Relative microelastic mapping of living cells by atomic force microscopy. *Biophys. J.* **1998**, 74 (3), 1564–1578.
- (27) Berdyyeva, T. K.; Woodworth, C. D.; Sokolov, I. Human epithelial cells increase their rigidity with ageing in vitro: direct measurements. *Phys. Med. Biol.* **2005**, 50 (1), 81–92.
- (28) Fischer-Cripps, A. C. A review of analysis methods for sub-micron indentation testing. *Vacuum* **2000**, 58 (4), 569–585.
- (29) Lu, Z. X.; Liu, L. T.; Qi, X. R. Development of small interfering RNA delivery system using PEI-PEG-APRPG polymer for antiangiogenic vascular endothelial growth factor tumor-targeted therapy. *Int. J. Nanomed.* **2011**, 6, 1661–1673.
- (30) Fang, T. H.; Chang, W. J.; Tsai, S. L. Nanomechanical characterization of polymer using atomic force microscopy and nanoindentation. *Microelectron. J.* **2005**, 36 (1), 55–59.
- (31) Cho, H. J.; Yoon, I. S.; Yoon, H. Y.; Koo, H.; Jin, Y. J.; Ko, S. H.; Shim, J. S.; Kim, K.; Kwon, I. C.; Kim, D. D. Polyethylene glycol-conjugated hyaluronic acid-ceramide self-assembled nanoparticles for targeted delivery of doxorubicin. *Biomaterials* **2012**, 33 (4), 1190–200.
- (32) VanLandingham, M.; Villarrubia, J.; Meyers, G. Recent progress in nanoscale indentation of polymers using the AFM. In *Proceedings of the Sem IX International Congress on Experimental Mechanics*; Soc Experimental Mechanics Inc: Bethel, 2000; pp 912–915.
- (33) Zhang, G.; Liu, Y.; Yuan, Q.; Zong, C.; Liu, J.; Lu, L. Dual modal in vivo imaging using upconversion luminescence and enhanced computed tomography properties. *Nanoscale* **2011**, 3 (10), 4365–71.
- (34) Tranchida, D.; Kiflie, Z.; Acierno, S.; Piccarolo, S. Nanoscale mechanical characterization of polymers by atomic force microscopy (AFM) nanoindentations: viscoelastic characterization of a model material. *Meas. Sci. Technol.* **2009**, 20 (9), 095702.
- (35) Tranchida, D.; Kiflie, Z.; Piccarolo, S. Viscoelastic recovery behavior following atomic force microscope nanoindentation of semicrystalline poly(ethylene). *Macromolecules* **2007**, 40 (20), 7366–7371.
- (36) Tranchida, D.; Piccarolo, S.; Loos, J.; Alexeev, A. Accurately evaluating Young's modulus of polymers through nanoindentations: A phenomenological correction factor to the Oliver and Pharr procedure. *Appl. Phys. Lett.* **2006**, 89 (17), 171905.
- (37) Tranchida, D.; Piccarolo, S. On the use of the nanoindentation unloading curve to measure the Young's modulus of polymers on a nanometer scale. *Macromol. Rapid Commun.* **2005**, 26 (22), 1800–1804.
- (38) Clifford, C. A.; Seah, M. P. Quantification issues in the identification of nanoscale regions of homopolymers using modulus measurement via AFM nanoindentation. *Appl. Surf. Sci.* **2005**, 252 (5), 1915–1933.
- (39) Withers, J. R.; Aston, D. E. Nanomechanical measurements with AFM in the elastic limit. *Adv. Colloid Interface Sci.* **2006**, 120 (1–3), 57–67.
- (40) Choi, K. Y.; Yoon, H. Y.; Kim, J. H.; Bae, S. M.; Park, R. W.; Kang, Y. M.; Kim, I. S.; Kwon, I. C.; Choi, K.; Jeong, S. Y.; Kim, K.; Park, J. H. Smart nanocarrier based on PEGylated hyaluronic acid for cancer therapy. *ACS Nano* **2011**, 5 (11), 8591–8599.
- (41) Pharr, G. M. Measurement of mechanical properties by ultra-low load indentation. *Mat. Sci. Eng. A-Struct. Mater. Prop. Microstruct. Processing* **1998**, 253 (1–2), 151–159.
- (42) Lu, H.; Wang, B.; Ma, J.; Huang, G.; Viswanathan, H. Measurement of creep compliance of solid polymers by nano-indentation. *Mech. Time-Dependent Mater.* **2003**, 7 (3–4), 189–207.
- (43) Oyen, M. L. Analytical techniques for indentation of viscoelastic materials. *Philos. Mag.* **2006**, 86 (33–35), 5625–5641.
- (44) Oyen, M. L.; Cook, R. F. Load-displacement behavior during sharp indentation of viscous-elastic-plastic materials. *J. Mater. Res.* **2003**, 18 (1), 139–150.
- (45) Napp, J.; Behnke, T.; Fischer, L.; Wurth, C.; Wottawa, M.; Katschinski, D. M.; Alves, F.; Resch-Genger, U.; Schaferling, M. Targeted luminescent near-infrared polymer-nanoprobes for in vivo imaging of tumor hypoxia. *Anal. Chem.* **2011**, 83 (23), 9039–9046.
- (46) Corem-Salkmon, E.; Ram, Z.; Daniels, D.; Perlstein, B.; Last, D.; Salomon, S.; Tamar, G.; Shneor, R.; Guez, D.; Margel, S.; Mardor, Y. Convection-enhanced delivery of methotrexate-loaded maghemite nanoparticles. *Int. J. Nanomed.* **2011**, 6, 1595–602.

- (47) Derjaguin, B. V.; Muller, V. M.; Toporov, Y. P. Effect of contact deformations on the adhesion of particles. *J. Colloid Interface Sci.* **1975**, *53* (2), 314–326.
- (48) Johnson, K. L.; Kendall, K.; Roberts, A. D. Surface Energy and the Contact of Elastic Solids. *Proc. R. Soc. London, A: Math. Phys. Sci.* **1971**, *324* (1558), 301–313.
- (49) Sergici, A. O.; Adams, G. G.; Muftu, S. Adhesion in the contact of a spherical indenter with a layered elastic half-space. *J. Mech. Phys. Solids* **2006**, *54* (9), 1843–1861.
- (50) Fischer-Cripps, A. C., *Introduction to contact mechanics*. 2nd ed.; Springer: New York, 2007; p xxi, 221 p.
- (51) Grierson, D. S.; Flater, E. E.; Carpick, R. W. Accounting for the JKR–DMT transition in adhesion and friction measurements with atomic force microscopy. *J. Adhes. Sci. Technol.* **2005**, *19* (3–5), 291–311.
- (52) Wu, K. C.; You, H. I. Determination of solid material elastic modulus and surface energy based on JKR contact model. *Appl. Surf. Sci.* **2007**, *253* (20), 8530–8537.
- (53) Alderighi, M.; Ierardi, V.; Fuso, F.; Allegrini, M.; Solaro, R. Size effects in nanoindentation of hard and soft surfaces. *Nanotechnology* **2009**, *20* (23), 235703.
- (54) Briscoe, B. J.; Sebastian, K. S.; Adams, M. J. The Effect of Indenter Geometry on the Elastic Response to Indentation. *J. Phys. D: Appl. Phys.* **1994**, *27* (6), 1156–1162.
- (55) Hou, H. Y.; Chang, N. K.; Chang, S. H. Dynamic indentation of polymers using the atomic force microscope. *Nanomech. Mater. Struct.* **2006**, 171–180.
- (56) Jiang, X.; Sha, X.; Xin, H.; Chen, L.; Gao, X.; Wang, X.; Law, K.; Gu, J.; Chen, Y.; Jiang, Y.; Ren, X.; Ren, Q.; Fang, X. Self-aggregated pegylated poly (trimethylene carbonate) nanoparticles decorated with c(RGDyK) peptide for targeted paclitaxel delivery to integrin-rich tumors. *Biomaterials* **2011**, *32* (35), 9457–9469.
- (57) Arsenlis, A.; Parks, D. M. Crystallographic aspects of geometrically-necessary and statistically-stored dislocation density. *Acta Mater.* **1999**, *47*, 1597–1611.
- (58) Sader, J. E.; Larson, I.; Mulvaney, P.; White, L. R. Method for the Calibration of Atomic-Force Microscope Cantilevers. *Rev. Sci. Instrum.* **1995**, *66* (7), 3789–3798.
- (59) Cumpson, P. J.; Hedley, J. Accurate analytical measurements in the atomic force microscope: a microfabricated spring constant standard potentially traceable to the SI. *Nanotechnology* **2003**, *14* (12), 1279–1288.
- (60) Cumpson, P. J.; Zhdan, P.; Hedley, J. Calibration of AFM cantilever stiffness: a microfabricated array of reflective springs. *Ultramicroscopy* **2004**, *100* (3–4), 241–251.
- (61) Clifford, C. A.; Seah, M. P. The determination of atomic force microscope cantilever spring constants via dimensional methods for nanomechanical analysis. *Nanotechnology* **2005**, *16* (9), 1666–1680.
- (62) Tortonese, M.; Kirk, M. Characterization of application specific probes for SPMs. *Micromach. Imaging* **1997**, *3009*, 53–60.
- (63) Sokolov, I.; Ong, Q. K.; Shodiev, H.; Chechik, N.; James, D.; Oliver, M. AFM study of forces between silica, silicon nitride and polyurethane pads. *J. Colloid Interface Sci.* **2006**, *300* (2), 475–481.
- (64) King, R. B. Elastic analysis of some punch problems for a layered medium. *Int. J. Solids Struct.* **1987**, *23* (12), 1657–1664.
- (65) El-Sayed, A.; Masuda, T.; Akita, H.; Harashima, H. Stearylated INF7 peptide enhances endosomal escape and gene expression of PEGylated nanoparticles both in vitro and in vivo. *J. Pharm. Sci.* **2012**, *101* (2), 879–882.
- (66) Diaconu, L.; Dorohoi, D. Properties of polyurethane thin films. *J. Optoelectron. Adv. Mater.* **2005**, *7* (2), 921–924.
- (67) Adkins, R. T. *Information sources in polymers and plastics*; Bowker-Saur: London and New York, 1989.
- (68) Kalpakjian, S.; Schmid, S. R., *Manufacturing processes for engineering materials*, 5th ed.; Pearson Education: Upper Saddle River, N.J., 2008.
- (69) Israelachvili, J. N. *Intermolecular and surface forces: with applications to colloidal and biological systems*; Academic Press: London and Orlando, FL, 1985.
- (70) Tabor, D. Surface forces and surface interactions. *J. Colloid Interface Sci.* **1977**, *58* (1), 2–13.
- (71) Sahib, M. N.; Darwis, Y.; Peh, K. K.; Abdulameer, S. A.; Tan, Y. T. Rehydrated sterically stabilized phospholipid nanomicelles of budesonide for nebulization: physicochemical characterization and in vitro, in vivo evaluations. *Int. J. Nanomed.* **2011**, *6*, 2351–2366.
- (72) Zhan, C.; Meng, Q.; Li, Q.; Feng, L.; Zhu, J.; Lu, W. Cyclic RGD-polyethylene glycol-polyethylenimine for intracranial glioblastoma-targeted gene delivery. *Chem. Asian J.* **2012**, *7* (1), 91–96.
- (73) Jin, J.; Bae, K. H.; Yang, H.; Lee, S. J.; Kim, H.; Kim, Y.; Joo, K. M.; Seo, S. W.; Park, T. G.; Nam, D. H. In vivo specific delivery of c-Met siRNA to glioblastoma using cationic solid lipid nanoparticles. *Bioconjugate Chem.* **2011**, *22* (12), 2568–2572.
- (74) Xing, H.; Bu, W.; Zhang, S.; Zheng, X.; Li, M.; Chen, F.; He, Q.; Zhou, L.; Peng, W.; Hua, Y.; Shi, J. Multifunctional nanoprobe for upconversion fluorescence, MR and CT trimodal imaging. *Biomaterials* **2012**, *33* (4), 1079–1089.
- (75) Peng, C.; Zheng, L.; Chen, Q.; Shen, M.; Guo, R.; Wang, H.; Cao, X.; Zhang, G.; Shi, X. PEGylated dendrimer-entrapped gold nanoparticles for in vivo blood pool and tumor imaging by computed tomography. *Biomaterials* **2012**, *33* (4), 1107–1119.
- (76) Li, J.; Yang, Y.; Huang, L. Calcium phosphate nanoparticles with an asymmetric lipid bilayer coating for siRNA delivery to the tumor. *J. Controlled Release* **2011**.
- (77) Ngan, A. H. W.; Tang, B. Viscoelastic effects during unloading in depth-sensing indentation. *J. Mater. Res.* **2002**, *17* (10), 2604–2610.